Celestial Mechanics and Dynamical Astronomy manuscript No.
(will be inserted by the editor)

arXiv:1403.3072v1 [astro-ph.EP] 12 Mar 2014

H. A. Folonier · F. Roig · C. Beaugé

Capture Probability in the 3:1 Mean Motion Resonance with Jupiter

An Application to the Vesta Family

Received: / Accepted:

Abstract We study the capture and crossing probabilities into the 3:1 mean motion resonance with Jupiter for a small asteroid that migrates from the inner to the middle Main Belt under the action of the Yarkovsky effect. We use an algebraic mapping of the averaged planar restricted three-body problem based on the symplectic mapping of Hadjidemetriou (1993), adding the secular variations of the orbit of Jupiter and non-symplectic terms to simulate the migration. We found that, for fast migration rates, the captures occur at discrete windows of initial eccentricities whose specific locations depend on the initial resonant angles, indicating that the capture phenomenon is not probabilistic. For slow migration rates, these windows become narrower and start to accumulate at low eccentricities, generating a region of mutual overlap where the capture probability tends to 100%, in agreement with the theoretical predictions for the adiabatic regime. Our simulations allow to predict the capture probabilities in both the adiabatic and non-adiabatic cases, in good agreement with results of Gomes (1995) and Quillen (2006). We apply our model to the case of the Vesta asteroid family in the same context as Roig et al (2008), and found results indicating that the high capture probability of Vesta family members into the 3:1 mean motion resonance is basically governed by the eccentricity of Jupiter and its secular variations.

Keywords Asteroids · Resonances · Capture probabilities · Adiabatic migration · Symplectic mappings · V-type asteroids

1 Introduction

Asteroid taxonomy classify the asteroids in different types according to the characteristics of their reflectance colors and/or spectra (e.g. Tholen 1984; Bus and Binzel 2002; DeMeo et al 2009). V-type asteroids are a particular class whose reflectance spectra have been recognized to be compatible with the spectra of the basaltic achondritic meteorites (e.g. Binzel and Xu 1993; Hiroi and Pieters 1998; Burbine et al 2001). Currently, the only known source for these asteroids is the Vesta family (e.g. Migliorini et al

H. A. Folonier
Instituto de Astronomia Geofísica e Ciências Atmosféricas, Universidade de São Paulo, Brasil
E-mail: folonier@usp.br

F. Roig
Observatório Nacional, Rio de Janeiro, Brasil
E-mail: froig@on.br

C. Beaugé
Instituto de Astronomía Teórica y Experimental (IATE), Observatorio Astronómico de Córdoba, Universidad Nacional de Córdoba, Argentina
E-mail: beauge@oac.uncor.edu

1997; Mothé-Diniz et al 2005) a group of asteroids in the inner Main Belt ($2.1 < a < 2.5$ AU) which constitute the outcome of a collision that excavated the basaltic surface of asteroid (4) Vesta more than 1 Gyr ago (e.g. McCord et al 1970; Thomas et al 1997; Asphaug 1997). Although most of the V-type asteroids, the so called vestoids, are found within the limits of the Vesta family ($2.22 < a < 2.47$ AU), several V-type bodies are also found far away from the family outskirts (e.g. Cruikshank et al 1991; Lazzaro et al 2000; Roig et al 2008; Moskovitz et al 2008b; Duffard and Roig 2009), which raises the question of how these asteroids get to their current locations. Among the suggested mechanisms, Roig et al (2008) show that some V-type asteroids initially in the Vesta family would be able to cross the 3:1 mean motion resonance (MMR) with Jupiter (hereafter J3:1) at 2.5 AU to get to the middle Main Belt ($2.5 < a < 2.8$ AU). The crossing would be driven by a slow migration of the orbital semimajor axis induced by the thermal emission forces on the asteroid's surface, the so called Yarkovsky effect (e.g. Bottke et al 2002). Inspired by this result, we address here the problem of resonance crossing/capture in the case of the J3:1 MMR from a wider perspective, aiming to investigate how this phenomenon happens and how the results of Roig et al (2008) can be interpreted in the light of the general resonance crossing/capture mechanism.

Different authors have proposed different dynamical mechanisms to explain, at least partially, the presence of V-type asteroid in the inner Main Belt beyond the domains of the Vesta family. Carruba et al (2005) showed that some V-type asteroids could have migrated from the Vesta family to their current orbits due to the interplay between the Yarkovsky effect and non-linear secular resonances. Nesvorný et al (2008) addressed a similar interplay, but with two-body and three-body MMRs. Even the role close encounter with massive asteroids has also been proposed as a mechanism (Carruba et al 2007; Delisle and Laskar 2012). However, these mechanisms are not sufficient to account for all the V-type asteroids found in the inner Main Belt.

To add to the puzzle, several V-type candidates have been recently discovered in the middle Main Belt (e.g. Roig and Gil-Hutton 2006; Moskovitz et al 2008a), and although most of them still lack spectroscopic confirmation, they are strong photometric candidates. Some of these bodies have moderate sizes, with diameters between 2-5 km, and their origin is still a matter of debate. For the time being, the only reliable source of these asteroids should be the Vesta family. However, in order to reach their present locations, these asteroids should have crossed the J3:1 MMR which, at first hand, appears a near impossible task due to the strong chaotic behavior that a small asteroid temporarily trapped in this MMR would experiment. Actually, it is well known that even in the simplest models, the J3:1 resonant motion drives asteroids to high- and very high-eccentricity orbits in less than a few tens of million years (Wisdom 1982; Ferraz-Mello and Klafke 1991; Ferraz-Mello et al 1996). This behavior allows the asteroids to cross the orbits of Mars and of the Earth, thus being removed by close encounters with these planets. Roig et al (2008), used full N-body simulations, including the perturbations of all the planets from Venus to Neptune, to find that for asteroids with diameter of the order of 0.1-1.0 km there is a small probability ($\sim 3\%$) of crossing this resonance going from the inner to the middle Main Belt. For larger bodies, the probability would be even lower. In principle, the results of Roig et al (2008) could only explain very few cases of V-type candidates in the middle Main Belt.

The above scenario raises some questions like: Is the interaction with the J3:1 MMR enough to explain other V-type candidates? How does the resulting evolution depend on the asteroid's size? What dynamical effects are relevant to the crossing/capture probability? Would other planetary configurations lead to different results? These questions shift the spotlight from the origin of the V-type asteroids to a more fundamental issue: What is the capture/crossing probability in the J3:1 MMR? And how does this vary in different dynamical models and migration regimes?

The problem of resonance trapping has been approached by many authors. Neishtadt (1975) presented one of the first studies of passages through a resonance separatrix with a slowly-varying parameter (i.e. adiabatic regime). Yoder (1979) calculated the capture probability in the case of a simple pendulum, while Henrard (1982) extended the study to the second fundamental model for first-order resonances. The case of higher-order commensurabilities was undertaken by Lemâitre (1984) and by Borderies and Goldreich (1984). Finally, Malhotra (1990) analyzed the capture in secondary resonances including mutual inclination between the asteroid and the perturbing planet.

All these works, however, deal with the adiabatic case in which the migration timescale towards the resonance is much longer than the libration period. For very small asteroids, however, the Yarkovsky effect may lead to a non-adiabatic migration (e.g. Farinella et al 1998; Vokrouhlický and Farinella 2000), and many of the classical predictions by the above authors may not be valid. The problem

of resonance capture/crossing under a non-adiabatic regime is still little understood. Gomes (1995) studied the evolution of small particles migrating due to the Poynting-Robertson drag. He found that the capture probability decreases for increasing migration rates, especially for almost circular orbits. A similar result was also found by Quillen (2006), who addressed the case where the migrating body is the perturber. In particular, this author introduces a simple semi-analytical model which allows her to study the capture probability in a single MMR of any order and also in the occurrence of a secondary resonance. Recently, Mustill and Wyatt (2011) used a Hamiltonian model to investigate the capture probabilities in first and second order resonances considering different scenarios like planet migration through a gas disk, through a debris disk, and also dust migration under the Poynting-Robertson drag. These authors found that resonant capture fails for high migration rates, and has decreasing probability for higher eccentricities, although for certain migration rates, capture probability peaks at a finite eccentricity. They also found that more massive planets can capture particles at higher eccentricities and migration rates.

In this work we focus on the behavior of convergent migration towards the J3:1 MMR due to the Yarkovsky effect, both in the adiabatic and non-adiabatic regimes. We are particularly interested in three key issues: (i) how the capture probability changes with the migration rate, (ii) the effects of different dynamical models, and (iii) an application of these results to the Vesta family. We are also interested in the behavior of the dynamical system for a wide range of migration rates, and consequently will also discuss drifts that correspond to meteoroid-size bodies. Since the orbital evolution of such small particles is also influenced by other physical processes (e.g. YORP, spin reorientations, etc), our results for this high non-adiabatic regime should not be considered as accurate predictions, but solely for theoretical completeness.

The paper is organized as follows. In Sect. 2, we present our dynamical model and equations of motion. In Sect. 3, we introduce an algebraic mapping that allows us to follow the evolution of a huge number of sets of initial conditions with less computational cost. The probability of resonance capture in the adiabatic and non-adiabatic cases is discussed in Sect. 4. Numerical simulations with our mapping in both adiabatic and non-adiabatic regimes are presented in Sect. 5. An application of our results to the present-day distribution of V-type asteroids is given in Sect. 6. Finally, conclusions close the paper in Sect. 7.

2 The Dynamical Model

Our analysis is based on a planar restricted three-body problem, consisting of a massless particle (asteroid) orbiting a primary of mass m_0 (Sun) and perturbed by an exterior mass m_1 (Jupiter). We adopt the usual Delaunay canonical variables:

$$\begin{aligned} L &= \sqrt{\mu a}, & \lambda &= \text{mean longitude}, \\ L-G &= \sqrt{\mu a}(1-\sqrt{1-e^2}), & -\varpi &= \text{longitude of pericenter}, \end{aligned} \tag{1}$$

where $\mu = \mathcal{G}m_0$, $\mathcal{G}$ is the gravitational constant, a is the semimajor axis of the asteroid and e its eccentricity. The orbital elements of the perturbing mass (Jupiter) will be denoted by a subscript 1. The mean motions will be denoted by n and n_1, respectively. Orbital elements are assumed to be heliocentric.

In these variables, the Hamiltonian governing the orbital evolution of the asteroid is given by the expression:

$$\mathcal{H} = -\frac{\mu^2}{2L^2} + n_1\Lambda - \frac{\mu_1}{a_1}\, R(L, L-G, \Lambda, \lambda, \varpi, \lambda_1), \tag{2}$$

where R is the disturbing function, $\mu_1 = \mathcal{G}m_1$ and Λ is the canonical momentum associated to $\lambda_1 = n_1 t$.

Restricting the phase space to a vicinity of the J3:1 MMR, we can expand R in a Fourier-Poisson series (e.g. Laplace expansion) and average over the short-period terms. Performing this averaging up to first order in the masses, and retaining only terms up to second order in the eccentricities, we can write the resonant Hamiltonian as:

$$\mathcal{H} = -\frac{\mu^2}{2L^2} + n_1\Lambda -$$

$$-\frac{\mu_1}{a_1}\left[e^2 A_1 + e e_1 A_3 \cos(\varpi - \varpi_1) + e^2 A_5 \cos(3\lambda_1 - \lambda - 2\varpi) + \right.$$
$$\left. + e e_1 A_6 \cos(3\lambda_1 - \lambda - \varpi - \varpi_1) + e_1^2 A_7 \cos(3\lambda_1 - \lambda - 2\varpi_1)\right], \quad (3)$$

where, for simplicity, we have kept the same notation used for the original Hamiltonian functions. In this expression A_i are function of the Laplace coefficients $b_s^{(j)}(a/a_1)$ and are considered constant. According to Murray and Dermott (1999) their values at the J3:1 MMR ($a/a_1 = 0.48075$) are:

$$A_1 = 0.142097, \qquad A_3 = -0.165406, \qquad A_5 = 0.598100,$$
$$A_6 = -2.21124, \qquad A_7 = 0.362954.$$

Since we are interested in the motion around the J3:1 commensurability, we may transform our variables to their resonant counterparts (e.g. Henrard and Lemâitre 1983):

$$\begin{aligned} \sigma &= \frac{1}{2}(3\lambda_1 - \lambda) - \varpi, & S &= (L - G), \\ -\nu &= \frac{1}{2}(3\lambda_1 - \lambda) - \varpi_1, & N &= (L - G) - L - \Lambda, \\ Q &= \frac{1}{2}(\lambda_1 - \lambda), & \bar{\Lambda} &= -\Lambda - 3L. \end{aligned} \quad (4)$$

As the averaged Hamiltonian does not depend explicitly on Q, its momentum $\bar{\Lambda}$ is a constant of motion. Without any loss in generality we can take its value equal to zero, from which we can attain that $\Lambda = -3L$. In this manner, the system is reduced to 2 degrees of freedom and the remaining canonical momenta acquire the form:

$$S = (L - G) = \sqrt{\mu a}\left(1 - \sqrt{1 - e^2}\right),$$
$$N = (L - G) + 2L = \sqrt{\mu a}\left(3 - \sqrt{1 - e^2}\right). \quad (5)$$

Finally, since we are only retaining terms in R up to the second order in the eccentricities, we can write e as a function of both S and N up to the same order as:

$$e \approx 2\sqrt{\frac{S}{N}}. \quad (6)$$

Writing the resonant Hamiltonian Eq. (3) in terms of the resonant canonical variables, we obtain, up to the second order in the eccentricities:

$$\mathcal{H} = -\frac{2\mu^2}{(N-S)^2} - \frac{3}{2}n_1(N - S) - \frac{\mu_1}{a_1}\left[4\frac{S}{N}\left(A_1 + A_5\cos(2\sigma)\right) + \right.$$
$$\left. + 2e_1\sqrt{\frac{S}{N}}\left(A_3\cos(\sigma + \nu) + A_6\cos(\sigma - \nu)\right) + e_1^2 A_7\cos(2\nu)\right]. \quad (7)$$

The resulting equations of motion can be explicitly written as:

$$\begin{aligned} \frac{dS}{dt} &= -\frac{\mu_1}{a_1}\frac{8S}{N}A_5\sin(2\sigma) - \frac{\mu_1}{a_1}2e_1\sqrt{\frac{S}{N}}\left[A_3\sin(\sigma + \nu) + A_6\sin(\sigma - \nu)\right] \\ \frac{dN}{dt} &= -\frac{\mu_1}{a_1}2e_1^2 A_7\sin(2\nu) - \frac{\mu_1}{a_1}2e_1\sqrt{\frac{S}{N}}\left[A_3\sin(\sigma + \nu) - A_6\sin(\sigma - \nu)\right] \\ \frac{d\sigma}{dt} &= -\frac{4\mu^2}{(N-S)^3} + \frac{3}{2}n_1 - \frac{\mu_1}{a_1}\frac{4}{N}\left[A_1 + A_5\cos(2\sigma)\right] - \\ &\quad -\frac{\mu_1}{a_1}\frac{e_1}{\sqrt{S\,N}}\left[A_3\cos(\sigma + \nu) + A_6\cos(\sigma - \nu)\right] \\ \frac{d\nu}{dt} &= \frac{4\mu^2}{(N-S)^3} - \frac{3}{2}n_1 + \frac{\mu_1}{a_1}\frac{4S}{N^2}\left[A_1 + A_5\cos(2\sigma)\right] + \\ &\quad +\frac{\mu_1}{a_1}e_1\sqrt{\frac{S}{N^3}}\left[A_3\cos(\sigma + \nu) + A_6\cos(\sigma - \nu)\right]. \end{aligned} \quad (8)$$

3 The Algebraic Mapping

To solve these variational equations, we implemented an algebraic mapping based on the symplectic mapping introduced by Hadjidemetriou (1986, 1991, 1993) and by Ferraz-Mello (1996), to which we added a non-symplectic term (e.g. Cordeiro et al 1996) simulating the migration due to the Yarkovsky effect.

The classical Hadjidemetriou's mapping is a variation of the twist map, tailored to preserve the fixed points of the original Hamiltonian as well as their stability indices. If we write the averaged Hamiltonian Eq. (7) as:

$$\mathcal{H}(\boldsymbol{I},\boldsymbol{\theta}) = \mathcal{H}_0(\boldsymbol{I}) + \mu_1 \mathcal{H}_1(\boldsymbol{I},\boldsymbol{\theta}), \tag{9}$$

where $(\boldsymbol{I},\boldsymbol{\theta}) \equiv (S,N,\sigma,\nu)$, $\mathcal{H}_0$ is the integrable part and $\mathcal{H}_1$ is the disturbing function, the mapping at the i-th step is given by a canonical transformation $(\boldsymbol{I}_i,\boldsymbol{\theta}_i) \rightarrow (\boldsymbol{I}_{i+1},\boldsymbol{\theta}_{i+1})$ with a Jacobi-type generating function:

$$\mathcal{S}(\boldsymbol{I}_{i+1},\boldsymbol{\theta}_i) = \boldsymbol{I}_{i+1}\cdot\boldsymbol{\theta}_i + \tau\mathcal{H}(\boldsymbol{I}_{i+1},\boldsymbol{\theta}_i). \tag{10}$$

From this expression, the implicit form of the mapping is given by:

$$\begin{aligned} \boldsymbol{I}_i &= \frac{\partial\mathcal{S}}{\partial\boldsymbol{\theta}_i} = \boldsymbol{I}_{i+1} + \tau\frac{\partial\mathcal{H}(\boldsymbol{I}_{i+1},\boldsymbol{\theta}_i)}{\partial\boldsymbol{\theta}_i}, \\ \boldsymbol{\theta}_{i+1} &= \frac{\partial\mathcal{S}}{\partial\boldsymbol{I}_{i+1}} = \boldsymbol{\theta}_i + \tau\frac{\partial\mathcal{H}(\boldsymbol{I}_{i+1},\boldsymbol{\theta}_i)}{\partial\boldsymbol{I}_{i+1}}. \end{aligned} \tag{11}$$

The time-step τ of the mapping must be set to the period of the synodic angle Q over which the Hamiltonian was averaged; see Hadjidemetriou (1993) for a detailed construction. This is $\tau = 2\pi/n_1 \approx 11.86$ yr, that corresponds to Jupiter's orbital period. Substituting the partial derivatives by the left-hand part of Eqs. (8), leads to the expression of the mapping for the J3:1 MMR. It is worth noting that the two equations for the actions $\boldsymbol{I} \equiv (S,N)$ are given in implicit form and must be solved iteratively before solving the two equations for the angles $\boldsymbol{\theta} \equiv (\sigma,\nu)$.

3.1 Adding the Yarkovsky Effect

The next step is to add to the algebraic mapping a non-conservative term mimicking the Yarkovsky effect acting on small asteroids. The main consequence of the Yarkovsky effect is a secular drift of the semimajor axis of the asteroid, but no changes in either the eccentricity or the angles. In other words, the total time variation of the semimajor axis can be expressed as the sum of two components:

$$\dot{a} = \dot{a}_G + \dot{a}_Y, \tag{12}$$

where $\dot{a}_G$ is due to the purely gravitational perturbations, while $\dot{a}_Y$ is the variation due to the non-conservative term.

According to Vokrouhlický (1999), the rate of change of the semimajor axis due to the diurnal version of the Yarkovsky effect can be given approximately by:

$$\dot{a}_Y = \kappa_d \frac{1\,\mathrm{km}}{D}\cos\epsilon, \tag{13}$$

where D is the diameter of the asteroid in km, ϵ is the obliquity of the spin axis with respect to the orbital plane, and κ_d is a constant that depends on several physical and thermal parameters of the asteroid, like the albedo, the surface thermal conductivity, the surface and bulk densities, the surface emissivity, and the rotational period. Assuming values of these quantities typical of the vestoids, we have $\kappa = 2.5\times10^{-10}$ AU/yr (e.g. Nesvorný et al 2008). We note that, if $\cos\epsilon > 0$, the asteroid increases its semimajor axis and pulls away from the Sun, while if $\cos\epsilon < 0$, it suffers an orbital decay. Since we wish to study convergent migration towards the J3:1 MMR from smaller values of the semimajor

axis, we assume $\cos\epsilon = 1$ in order to maximize the effect[1]. For the rest of this paper, we will apply Eq. (13) as an approximate link between a given migration rate and the corresponding asteroid diameter. Since the value of κ_d has been estimated from large vestoids, it is not clear that its value will remain invariant for smaller asteroids and meteoroids. However, our aim is not to give quantitatively accurate values of the body diameters, but to present illustrative quantities.

From Eqs. (5), we can see that both canonical momenta depend on the semimajor axis, so both will be affected by the Yarkovsky effect, that is:

$$\dot{\boldsymbol{I}} = \frac{\partial \boldsymbol{I}}{\partial a}\dot{a} + \frac{\partial \boldsymbol{I}}{\partial e}\dot{e} = \left(\frac{\partial \boldsymbol{I}}{\partial a}\dot{a}_G + \frac{\partial \boldsymbol{I}}{\partial e}\dot{e}\right) + \frac{\partial \boldsymbol{I}}{\partial a}\dot{a}_Y, \tag{14}$$

and taking into account that $\boldsymbol{I} = \sqrt{\mu a}\,\Phi(e)$, we have:

$$\dot{\boldsymbol{I}} = \dot{\boldsymbol{I}}_G + \frac{2\mu \boldsymbol{I}}{(N-S)^2}\dot{a}_Y, \tag{15}$$

where $\dot{\boldsymbol{I}}_G$ is given by the first two Eqs. (8).

Introducing this expression into the mapping, we obtain:

$$\begin{aligned} \boldsymbol{I}_{i+1} &= \boldsymbol{I}_i - \tau\mu_1 \frac{\partial \mathcal{H}_1(\boldsymbol{I}_{i+1}, \boldsymbol{\theta}_i)}{\partial \boldsymbol{\theta}_i} + \tau\dot{a}_Y \frac{2\mu \boldsymbol{I}_{i+1}}{(N_{i+1} - S_{i+1})^2}, \\ \boldsymbol{\theta}_{i+1} &= \boldsymbol{\theta}_i + \tau \frac{\partial \mathcal{H}_0(\boldsymbol{I}_{i+1})}{\partial \boldsymbol{I}_{i+1}}. + \tau\mu_1 \frac{\partial \mathcal{H}_1(\boldsymbol{I}_{i+1}, \boldsymbol{\theta}_i)}{\partial \boldsymbol{I}_{i+1}}. \end{aligned} \tag{16}$$

It is worth noting that the addition of the Yarkovsky term breaks the symplectic structure of the original mapping at $\boldsymbol{I}_{i+1}$ or at $\boldsymbol{I}_i$. This is not a problem since the Yarkovsky effect acts as a dissipation, thus we should not expect the conservation of the Hamiltonian $\mathcal{H}$. Note also that, if $\dot{a}_Y > \mu_1$, the non-conservative term may become as important as the gravitational perturbation itself. In our simulations, we always consider drift values such that $\dot{a}_Y < \mu_1$.

3.2 Adding Long Period Terms of the Perturber's Orbit

Following Ferraz-Mello (1996) and Roig and Ferraz-Mello (1999), the mapping can be further improved by adding the secular perturbations on the orbit of Jupiter. From the classical planetary theory, we have that the secular change of the eccentricity e_1 and perihelion longitude ϖ_1 is given by a sum of harmonic terms:

$$e_1 \exp \mathrm{i}\varpi_1 = \sum_k G_k \exp[\mathrm{i}(\gamma_k t + \phi_k)] \qquad\qquad \mathrm{i} = \sqrt{-1}. \tag{17}$$

The values for the amplitudes G_k, frequencies γ_k, and initial phases ϕ_k of the harmonics are listed in Table 1, and they were adopted from the synthetic secular theory LONGSTOP 1B (Nobili et al 1989). In particular, we considered only the principal harmonics, i.e. those with amplitude $G_k \geq 10^{-4}$. The only exceptions are the harmonics g_8 and $2g_5 - g_6$, which are not excluded because g_8 is one of the fundamental frequencies of the planetary theory, and $2g_5 - g_6$ is the retrograde frequency of Jupiter's perihelion with the longest period. Equation (17) is directly introduced at each time step of the mapping, $t = i\tau$, through e_1 and ν in the right-hand part of Eqs. (8) and (16).

[1] There is also a seasonal version of the effect which produces a drift of the form:

$$-\kappa_s \frac{1\,\mathrm{km}}{D} \sin^2\epsilon,$$

but for the problem in hand, the constant $\kappa_s \ll \kappa_d$, thus the seasonal effect can be disregarded.

Table 1: Frequencies γ_k, initial phases ϕ_k and amplitudes G_k for the secular variation of Jupiter's orbit. Initial phases are given at JD 2440400.5. As usual, g_i, s_i represent the fundamental frequencies of the perihelia and nodes, respectively, of the planets (5 for Jupiter, 6 for Saturn, and so on).

Harmonic term	γ_k["/yr]	ϕ_k[°]	G_k	Period [yr]
g_5	4.25749319	27.0005	4.41872×10^{-2}	3.0440×10^5
g_6	28.24552984	124.1994	-1.57002×10^{-2}	4.5883×10^4
g_7	3.08675577	117.0516	1.8139×10^{-3}	4.1986×10^5
g_8	0.67255084	70.7508	5.80×10^{-5}	1.9270×10^6
$g_5 + g_6 - g_7$			-1.936×10^{-4}	4.4057×10^4
$-g_5 + g_6 + g_7$			1.982×10^{-4}	4.7867×10^4
$-g_5 + 2g_6$			-5.735×10^{-4}	2.4812×10^4
$2g_5 - g_6$			1.42×10^{-5}	-6.5685×10^4
$g_5 - s_6 + s_7$			1.104×10^{-4}	4.6940×10^4
$-g_5 + 2g_6 + s_6 - s_7$			-1.226×10^{-4}	4.4873×10^4

3.3 Comparison of the Mapping with the Full Hamiltonian Equations

In order to verify the validity of our mapping model, we performed a series of numerical simulations with the mapping and compared the results to those obtained from a direct N-body integration of the full Hamiltonian (Eq. 2), using a Bulirsch-Stoer integrator.

We chose 500 initial conditions in the $a - e$ plane over a line segment parallel to the left branch separatrix of the J3:1 MMR in the circular problem ($e_1 = 0$). Taking the initial angular variables as $\theta = 2\sigma = \pi$ and $\Delta\varpi = \sigma + \nu = \pi$, this line of initial conditions follows the equation $a = 2.49 - e/10$, with $0.01 \leq e \leq 0.4$. The orbital elements of Jupiter were fixed to $a_1 = 5.202545$ AU, $e_1 = 0$ or 0.048, $\varpi_1 = 0$, and $\lambda_1 = 0$.

We adopted three different values for the Yarkovsky drift rate $\dot{a}_Y$, corresponding to a very fast migration ($\dot{a}_Y = 5 \times 10^{-5}$ AU/yr; $D = 0.5$ cm), an intermediate migration ($\dot{a}_Y = 5 \times 10^{-6}$ AU/yr; $D = 5$ cm), and a slow migration ($\dot{a}_Y = 5 \times 10^{-7}$ AU/yr; $D = 50$ cm). The total integration time span was $T = 2.0 \times 10^3$, 2.0×10^4, and 2.0×10^5 yr, respectively for each drift rate. The time step of the N-body code was automatically adjusted to match a tolerance of 10^{-11} in the precision of the solution.

In Fig. 1, we show the results of this comparison for the circular case. The black V-shaped lines in the upper row panels are the separatrix of the circular problem, and the green line is the set of initial conditions. The red dots are the final conditions (at $t = T$) of the simulations obtained with the mapping, while the blue dots were obtained with the N-body integration. In the lower row panels, we show the final semimajor axes as a function of the initial eccentricity. The leftmost panels correspond to the fastest migration rate, while the rightmost ones correspond to the slowest rate.

We found a very good agreement between the mapping results and the N-body integrations, both showing the same structures of crossings and captures. For the fastest migration rates, the resonance captures appear to occur in certain discrete "windows" of initial eccentricities (lower left plot in Fig. 1). In other words, there exists certain intervals of the initial eccentricities for which capture always occurs, and other values for which a resonance crossing is guaranteed. *Thus, the outcome of the resonance passage is not probabilistic, but well defined and deterministic.*

This can be seen more clearly along a more detailed range of fast migration rates, as shown in Fig. 2. As the migration rate decreases, the number of capture windows increases and the windows become narrower. New windows start to appear at high eccentricities, while those already present shift to the lower values of e. It is worth noting that in Fig. 2 the initial angles were fixed to $\theta = 2\sigma = 0$ and $\Delta\varpi = \sigma + \nu = 0$. By comparing the panels in Figs. 1 and 2 corresponding to the same migration rate (5×10^{-5} AU/yr), it becomes evident that the precise location of the capture windows strongly depends on the initial angles θ and $\Delta\varpi$.

As we approach the adiabatic regime (Fig. 1, bottom middle and right), the capture windows tend to accumulate and overlap in the region $0 \leq e < e_c \approx 0.04$, leading to certain capture for all initial conditions in this eccentricity range. However, for $e > e_c$ the windows do not overlap but continue to reduce in width while their mutual separation decreases, tending to zero in the adiabatic limit and

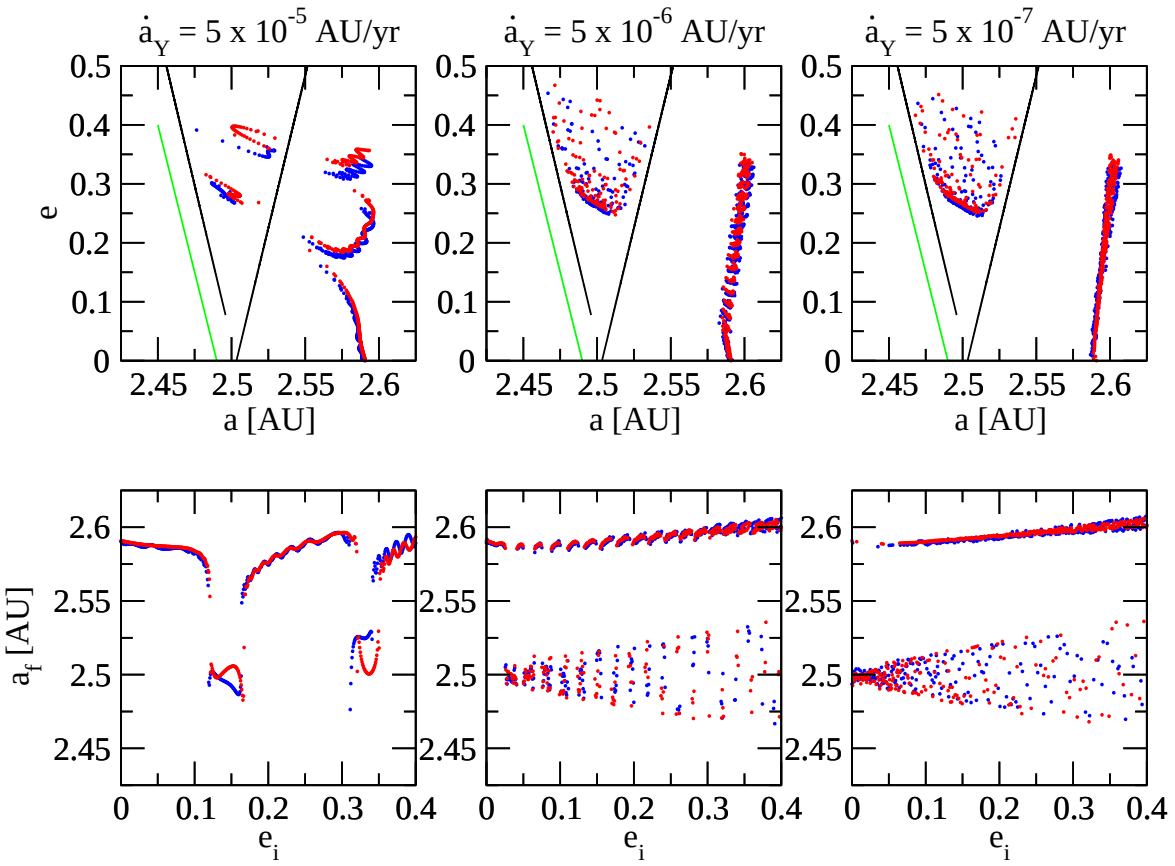

Fig. 1: Comparison between the algebraic mapping (red dots) and the integration of the full N-body equations (blue dots) in the circular case ($e_1 = 0$). The initial angles are set to $\theta = \Delta\varpi = \pi$. The migration rate decreases from left to right. *Top panels:* Final values of the semimajor axes and eccentricities. The green line represents the initial conditions, which are the same for both simulations. The separatrix of the resonance are shown for reference (black lines). *Bottom panels:* Final semimajor axes vs. initial eccentricities, where the structure of captures and crossing windows is appreciable (see also Fig. 2).

leading to a probabilistic treatment of the outcome of any initial condition. As we will show later, this behavior is in agreement with the resonance capture analytical model in the adiabatic regime.

Although these results assumed that the perturber is in a circular orbit, both the capture/crossing windows and their main characteristics are also observed in more complete dynamical models, such as the elliptic case and models including secular perturbations in the perturbing planet. Finally, it is worth noting that the computation time could be about 1,000 times faster with the mapping compared to an N-body integration. This allows to perform a huge amount of simulations with the mapping to obtain a statistically significant result.

3.4 Capture dependence on the initial angles

In this section, we investigate how the capture process depends on the initial angles, aiming to provide an explanation for the capture windows observed in Figs. 1 and 2. We considered a grid of test orbits with $a = 2.45$ AU and $e = 0.2$, and initial angles θ and $\Delta\varpi$ varying between 0 and 360°. These test orbits were integrated until either $a > 2.56$ AU (crossing) or $e > 0.5$ (capture).

The results are shown in Fig. 3, for three different Yarkovsky drift rates (the same shown in Fig. 1) and two different models: the circular problem (left panels) and the secular elliptic problem where the

eccentricity of Jupiter varies with time (right panels). The final fate of the orbits is identified by a blue color for crossings and white for captures. It is worth noting that the results for the pure elliptic model ($e_1 \neq 0$ fixed) are very similar to those of the secular elliptic model, being actually indistinguishable for the fastest drift rates.

Looking at the results for the circular model, which does not depend on $\Delta\varpi$, it is clear that the occurrences of captures are strongly dependent on the initial values of the resonant angle. This behavior can be explained by assuming that the capture takes place only if the orbit reaches the separatrix at, or very close to, the unstable (saddle) equilibrium point, which correspond to $\theta = 0$ in the J3:1 MMR. Since e remains almost constant before reaching the resonance region, the rate of circulation $\dot{\theta}$ depends primarily on the initial semimajor axis and all the test orbits reach the separatrix at approximately the same time τ. Therefore, for an initial angle θ_0, the evolution of θ upon reaching the separatrix is approximately given by $\theta - \theta_0 = \int_0^\tau \dot{\theta}(\dot{a}_Y t)\, dt$. Since the right-hand member is almost equal for all the orbits, only a limited range of θ_0 values could lead to $\theta \sim 0$ at the separatrix.

For the fast migration rates, $\tau \sim 300$ yr is smaller than the circulation period ($\dot{\theta} \lesssim 1,000$ yr), and the orbits reach the separatrix before they can complete a full circulation of the resonant angle. Thus, we should expect a limited number of capture windows. On the other hand, for the slowest migration rates, the orbits are able to make several circulations before reaching the separatrix ($\tau \sim 30,000$ yr), providing a larger number of capture windows. This produces the structure shown in the left panels of Fig. 3.

In the case of the elliptic models, the captures are still expected to occur through the saddle point $\theta = 0$, but the evolution is coupled with $\Delta\varpi$, which produces the complex patterns observed in the right panels of Fig. 3.

4 The Resonance Capture Probability

4.1 Adiabatic Case

Figure 4 (left) presents a schematic view of the phase space of a pendulum-type one degree of freedom dynamical system. We can define three domains: an inner circulation domain D_1 (in red), a libration domain D_2 (in blue), and an outer circulation domain D_3 (in white). We are interested in assessing the probability P_{ij} for an initial condition in region D_i to pass onto region D_j. Let J_i be the area of region D_i, such that $J_3 = J_1 + J_2$. In the absence of migration, these areas remain constant and only depend on the value of the momentum N, i.e. $J_i = J_i(N)$.

Following Henrard (1982), when a very slow migration is considered (adiabatic regime), the probability P_{3i} is given in a first approximation by:

$$P_{3i} = \frac{\partial J_i/\partial N}{\partial J_3/\partial N}. \tag{18}$$

This equation states that the capture probability is directly proportional to that ratio of the speed at which the areas D_i and D_3 change due to the migration. It is straightforward to show that $P_{31} = 1 - P_{32}$, since:

$$P_{31} + P_{32} = \frac{\partial J_1/\partial N}{\partial J_3/\partial N} + \frac{\partial J_2/\partial N}{\partial J_3/\partial N} = \frac{\partial (J_1 + J_2)/\partial N}{\partial J_3/\partial N} = 1, \tag{19}$$

To apply the above equation to the J3:1 MMR, we consider the Hamiltonian of the restricted circular three-body problem (Eq. (7); $e_1 = 0$) and, for each value of N, we numerically compute the values of J_1 and J_3, as well as their derivatives. A condition passing from region D_3 to D_2 constitutes a capture, while a condition passing from region D_3 to D_1 constitutes a crossing. Therefore, the capture probability is:

$$P_{cap} = P_{32}, \tag{20}$$

while the crossing probability is:

$$P_{cross} = P_{31} = 1 - P_{cap}. \tag{21}$$

To find P_{cap} as a function of N, we need to compute the ratio between the derivatives in Eq. (18). Since the Yarkovsky drift included in our model do not modify the eccentricity, we can replace N by

the value of e that the orbit has when it reaches the separatrix of the resonance. This allows us to study the capture probability directly as a function of e, as shown in the black curve of Fig. 4 (right).

These calculations indicate that, for eccentricities $0 \leq e < e_c \approx 0.05$, the capture probability is 100 %, while for $e > e_c$ it decays exponentially. In other words, for an adiabatic migration, any asteroid that enters the J3:1 MMR with $e < e_c$ will be captured. The capture probability reduces to less than 15 % for eccentricities larger than 0.4.

4.2 Non-Adiabatic Case

The capture probability in the non-adiabatic case is much more complex and little is known about its behavior. Probably the first general study was performed by Gomes (1995), who focused on the dynamics of small particles entering a MMR domain induced by the Poynting-Robertson effect. Using N-body numerical simulations, he found that, independently of the initial eccentricity, the capture probability decreased for faster migration rates. He also found that, in the non-adiabatic regime, the capture probability is zero for circular orbits, then increases up to certain maximum value at a given e_{max}, and then decreases again asymptotically to zero for higher eccentricities. The values of e_{max} and the corresponding maximum of P_{cap} depend on the migration rate: the faster the migration, the higher the e_{max} and the smaller the P_{cap}. This behavior is shown in Fig. 4 (right), which reproduces the curves estimated by Gomes (1995).

More recently, the non-adiabatic case has also been studied by Quillen (2006). A detailed discussion of her results in comparison with ours will be treated in Sect. 5.2.

5 Mapping Simulations

5.1 Capture Probability

In order to estimate the theoretical capture probability (in both the adiabatic and non-adiabatic regimes) with our mapping simulations, we considered three different models, depending on Jupiter's orbit: the circular model ($e_1 = 0$, hereafter CM), the elliptic model ($e_1 \neq 0$ fixed, hereafter EM), and the secular elliptic model (hereafter SEM) in which Jupiter's orbit feels the secular perturbations of the other major planets according to Eq. (17).

For the CM, we chose 1000 equispaced initial conditions over the line $a = 2.49 - \dfrac{e}{10}$, with $0.01 \leq e \leq 0.4$, parallel to the left branch of the separatrix of the (circular) J3:1 MMR in the $a - e$ plane. For each of these initial conditions, we considered 36 equispaced values of $\theta = 2\sigma$ between 0 and 2π. For the EM and SEM, we chose 100 initial values of (a, e) along the same lines, and for each of these we took 18×18 equispaced values of θ and $\Delta\varpi = \sigma + \nu$, both between 0 and 2π. It is worth noting that the proximity of these initial conditions to the resonance separatrix implies that the values of e upon reaching the separatrix are almost the same as their initial values. Therefore, from now on, we will analyze the capture probability directly as a function of the initial eccentricity of the orbits.

The initial conditions of Jupiter's orbit were $a_1 = 5.202545$ AU, $e_1 = 0$ for the CM, $e_1 = 0.048$ for the EM and SEM, $\lambda_1 = 0$ and $\varpi_1 = 0$. Each set of initial conditions was integrated with the mapping using 12 different migration rates $\dot{a}_Y$. In Table 2, we list these values together with the corresponding diameters according to Eq. (13). The Table also shows the total integration time span in each case, in units of mapping iterations, where each iteration has period τ.

In Figs. 5 and 6, we show the final semimajor axes as a function of the initial eccentricities for models CM and EM, respectively. The results of the secular elliptic model (SEM) shows no significant differences with those adopting a fixed orbit for the perturber, and are not shown. Each frame corresponds to a different migration rate, starting from the fastest (upper left) to the slowest (bottom right). We assume that an asteroid has crossed the resonance if its final semimajor axis is larger than a critical value, which varies from case to case but was always of the order of $a_c \approx 2.55$ AU. The capture conditions are represented in red, while the crossings are shown in blue. Since we have now considered an ensemble of initial angles $(\theta, \Delta\varpi)$, the windows associated to captures/crossing become blurred and there is no longer a predetermined outcome, even for fast migration rates.

Table 2: Assumed migration rates $\dot{a}_Y$ and their associated diameters D. The last three columns give the number of iteration steps used in the simulations of the different models. Each step corresponds to a period of ≈ 11.8 yr.

$\dot{a}_Y$ [AU/yr]	D [m]	CM	EM	SEM
5.0×10^{-4}	5.0×10^{-4}	35	90	90
2.5×10^{-4}	1.0×10^{-3}	90	100	100
1.0×10^{-4}	2.5×10^{-3}	150	150	150
5.0×10^{-5}	5.0×10^{-3}	200	250	250
2.5×10^{-5}	0.01	350	500	500
1.0×10^{-5}	0.025	700	1,000	1,000
5.0×10^{-6}	0.05	1,300	3,500	3,500
2.5×10^{-6}	0.1	2,500	10,000	15,000
1.0×10^{-6}	0.25	6,000	25,000	30,000
5.0×10^{-7}	0.5	12,500	60,000	75,000
2.5×10^{-7}	1.0	25,000	100,000	125,000
1.0×10^{-7}	2.5	60,000	300,000	300,000

The capture probability was computed by counting the number of captures that occur for each initial eccentricity and dividing it by the total number of initial conditions at that eccentricity. Rigorously speaking, the capture probability depends on the migration rate $\dot{a}_Y$, the initial value of e, and the initial angles θ and $\Delta\varpi$, as shown in Sect. 3.3. Since, for each eccentricity, the initial angles are varied between 0 and 2π, our counting method is equivalent to estimate an integrated probability:

$$\langle P_{cap} \rangle_{\theta,\Delta\varpi} = P_{cap}(e, \dot{a}_Y) = \frac{1}{(2\pi)^2} \int_0^{2\pi} \int_0^{2\pi} P_{cap}(e, \dot{a}_Y, \theta, \Delta\varpi)\ d\theta d\Delta\varpi. \tag{22}$$

The values of $P_{cap}(e, \dot{a}_Y)$ are shown in Fig. 7 for the CM (black curve), the EM (red curve), and the SEM (green curve).

At the fastest migration rate, all the initial conditions were able to cross the resonance in the CM, but in the EM and SEM a few captures were registered for large initial eccentricities ($e > 0.3$). Captures in the CM start to happen at migration rates slower than $\dot{a}_Y = 2.5 \times 10^{-4}$ AU/yr ($D = 0.1$ cm); however, in the EM and SEM captures already occur at lower eccentricities ($e > 0.2$) at the same migration rates. As expected, the capture windows appear initially at high eccentricities and move toward smaller e as the migration rate slows down (cf. Sect. 3.3).

At a migration rate of $\dot{a}_Y = 1.0 \times 10^{-5}$ AU/yr ($D = 2.5$ cm), the capture probability in the CM resembles the curve of a non-adiabatic capture (see Fig. 4), but with a lot of overlapped noise. This noise is introduced by the discretization of the capture windows, and it is not observed in Gomes (1995) since this author performed a smoothing of his capture curves. The capture probability starts with a maximum at large eccentricities, and drifts towards smaller eccentricities taking higher values as the migration rate becomes slower. In the EM and SEM, and for migration rates slower than $\dot{a}_Y = 5.0 \times 10^{-6}$ AU/yr ($D = 5$ cm), we observe a tail of final conditions that cross the resonance at low initial eccentricities (blue dots) This tail is formed by orbits that spent much more time inside the resonance than the remaining orbits before jumping it. This delay is probably due to the interaction of the orbits with secular and secondary resonances inside the MMR; that is why the same effect is not observed in the CM. At slower migration rates, this delay effect is observed for $0.05 < e < 0.25$.

For both the EM and SEM, the adiabatic regime starts for migration rates slower than $\dot{a}_Y = 1.0 \times 10^{-5}$ AU/yr ($D = 2.5$ cm), where the calculated probability resembles the theoretical curve predicted by Henrard's approach (see Fig. 4). For the CM, the adiabatic regime starts at even slower migration drifts, $\dot{a}_Y = 2.5 \times 10^{-7}$ AU/yr ($D = 1$ m). This means that in spite of the model, for real km-size asteroids the Yarkovsky drift should be considered as an adiabatic regime.

Finally, we observe that in the SEM, and for migration rates of $\dot{a}_Y = 5.0 \times 10^{-7}$ AU/yr ($D = 0.5$ m) and $\dot{a}_Y = 2.5 \times 10^{-7}$ AU/yr ($D = 1$ m), besides the tail of delayed orbits, there is a group of orbits whose final semimajor axes cluster around a value of $a = 2.82$ AU. This corresponds to the 5:2 MMR with Jupiter, which means that even if these orbits were able to dodge the J3:1 MMR, they did not circumvent the weaker J5:2 resonance.

5.2 Integrated Capture Probability

In the previous section, we have estimated the capture probability $P_{cap}(e, \dot{a}_Y)$ averaged over the angular variables θ and $\Delta\varpi$. To get an idea of the total capture probability as a function of the migration rate, we have to integrate the above estimate over an interval of eccentricity, i.e.:

$$\langle P_{cap} \rangle_e = P_{cap}(\dot{a}_Y) = \frac{1}{(0.4)} \int_0^{0.4} P_{cap}(e, \dot{a}_Y)\ de. \tag{23}$$

This is carried out by numerically integrating the curves shown in Fig. 7. The resulting probability $P_{cap}(\dot{a}_Y)$ is shown in Fig. 8 for the CM (black curve), the EM (green curve), and the SEM (red curve).

This result indicates that the total capture probability for asteroids with $0 \leq e \leq 0.4$ and slow migration rates is of the order of 40 % in the CM, and 30 % in the EM and SEM. However, as shown in Fig. 7, the adiabatic limit occurs for faster migrations in the EM and SEM rather than in the CM, and should lead to a 100 % capture probability for $e < e_c \approx 0.04$. If we divide the integral Eq. (23) in two sets, one in the interval $[0, e_c]$ and the other in the interval $[e_c, 0.4]$, we obtain the result shown in Fig. 9. As expected, at very low eccentricities, the capture probability tend to 100 % for faster migrations ($\dot{a}_Y = 5.0 \times 10^{-6}$ AU/yr; $D = 5$ cm) in the more realistic models than in the circular model ($\dot{a}_Y = 5.0 \times 10^{-7}$ AU/yr; $D = 50$ cm). On the other hand, for intermediate/large eccentricities, the capture probability is independent of the model adopted, and tends to 30 % in the adiabatic limit.

Before applying these results to the real case of the Vesta family and the vestoids, it is interesting to discuss our results with respect to those obtained by Quillen (2006). The main difference between Quillen's approach and ours is that she considers a fixed test particle with a migrating planet (and a migrating resonance), while we leave the planet fixed and migrate the test particle. In principle, both approaches should lead to the same result. However, Quillen did not report in her simulations the existence of the "capture windows" that we observe in our simulations. This is not surprising, since these structures appear when the initial angles of the orbits are fixed to the same value, as we showed in Sect. 3.4. Since Quillen (2006) chose initial random angles, the windows became hidden in her simulations. It is worth noting, however, that Quillen's procedure should not affect the computed capture probabilities, because she also averages the probabilities over the angular variables. Indeed, the curves shown in Fig. 9 resemble the behavior presented by Quillen (2006) in her figure 3. On the other hand, Mustill and Wyatt (2011) did detect the capture windows, but they did not provide a clear explanation for them.

This is a particularly important result, because Quillen's model is significantly different from ours. Although the basic Hamiltonian is the same in both models (i.e., an Andoyer-like Hamiltonian), she includes the non-conservative term directly as a variation of the mean motion of the planet $n_1 = n_1(t)$, that only affects the term of the unperturbed Hamiltonian that is linear in the actions. On the other hand, in our model, we include the non-conservative term as a repeated "kick" in the actions, so it does not only affect the linear term of the unperturbed Hamiltonian but also the quadratic term, as well as the amplitudes of the harmonics of the disturbing function. The fact that two models so different can lead to almost the same result demonstrates the robustness of the capture process.

6 Comparison with the Distribution of Real Asteroids

As a final task, we wish to find the integrated capture probability for V-type asteroids coming from the Vesta family (vestoids) as a function of the migration rate. Roig et al (2008) determine that the probability of a vestoid to cross the J3:1 MMR is of the order of 3 %. This result is based on numerical simulations of a full Solar System model (Venus to Neptune), including real Vesta family members close to the J3:1 resonance border as massless particles, and assigning to these asteroids two different drift rates: $\dot{a}_Y = 1.0 \times 10^{-10}$ AU/yr ($D = 2.5$ km) and $\dot{a}_Y = 1.0 \times 10^{-9}$ AU/yr ($D = 250$ m).

In principle, the Yarkovsky effect should only change the orbital semimajor axis of a Vesta family member, and thus it is expected that the Vesta family preserves more or less its original distribution in eccentricity. The interplay of the Yarkovsky effect with the many non-linear secular resonances and weak MMRs in inner Main Belt can produce significant variations of the Vesta family members' eccentricities (and inclinations) over Gyr time scales (e.g. Carruba et al 2005; Nesvorný et al 2008). However, these variations only affect a small fraction of the family members and will be disregarded

in our analysis. Figure 10 shows the location on the proper elements plane of the known Vesta family members. Assuming that over the interval of eccentricities of the Vesta family, that is approximately $0.07 \leq e_p \leq 0.14$, the proper eccentricity differs very little from the mean (i.e. averaged over the synodic perturbations) eccentricity, the integrated capture probability for the family becomes:

$$\langle P_{cap} \rangle_e = P_{Vesta}(\dot{a}_Y) = \frac{1}{0.07} \int_{0.07}^{0.14} P_{cap}(e, \dot{a}_Y)\ de. \tag{24}$$

Figure 11 shows the resulting probability for the different models. In the CM, the probability remains constant around 50 % for migration rates slower than $\dot{a}_Y = 5.0 \times 10^{-6}$ AU/yr ($D = 5$ cm). In the EM, the capture probability reaches 87 % for a migration rate of $\dot{a}_Y = 1.0 \times 10^{-9}$ AU/yr ($D = 250$ m), but the curve shows a growing tendency for smaller rates, and we may expect to get above 90 % for drift rates and order of magnitude slower. The behavior in the SEM is very similar to the EM, but with higher probabilities that may reach 95–96 % for the slowest rates simulated. These results are compatible with those obtained by Roig et al (2008), and imply that the very low probability that the vestoids have to cross the J3:1 MMR is basically due to the non-zero eccentricity of Jupiter. Therefore, it is not necessary to rely on the use of complex models or time consuming N-body simulations to efficiently reproduce this behavior.

7 Conclusions

In this work, we have studied the capture vs. crossing probability into the 3:1 mean motion resonance with Jupiter for an asteroid that migrates from the inner to the middle Main Belt under the action of a force that produces a secular change on its orbital semimajor axis. We were specially interested in the behavior of asteroids belonging to the Vesta family, that can migrate due to the thermal emission forces producing the so called Yarkovsky effect.

In order to perform a statistically significant analysis, we developed an algebraic mapping of the restricted three body problem, averaged over the synodic angle. The mapping is based on the symplectic approach developed by Hadjidemetriou (1993), but we add the secular variations on the orbit of the perturber, as well as non-symplectic terms to simulate the migration. The mapping has the advantage of being much faster than a full three-body high-order integration, but keeping the basic features of the behavior of the full model. This allowed us to perform a huge set of simulations with less computational cost. Moreover, the mapping model has the advantage that different parts of the model (eccentricity of Jupiter, secular variations, etc.) can be switched on and off, thus allowing us to analyze the relevance of these parts on the actual dynamics.

To simplify our study, we concentrated on three planar models (although the mapping could be easily extended to take into account the orbital inclinations of the bodies), according to the behavior of Jupiter's eccentricity: (i) circular model, (ii) elliptic model, and (iii) elliptic model with secular variations due to the other Jovian planets. The mapping results have been compared to numerical simulations of the full equations of motion for the circular and elliptic models, obtaining a very good agreement.

At very fast migration rates, most of the asteroids cross the resonance, while the few that are captured have initial eccentricities within a given range or "window". As the migration rate slows down, this window shifts to smaller eccentricities and becomes narrower, while new, even narrower, windows start to appear at higher eccentricities. At very slow migration rates, the shift of the windows to smaller eccentricities produces and accumulation of them, and their mutual overlap generates a region of very low e where the capture probability is 100 %, in agreement with the theoretical predictions.

Using the mapping, we have performed simulations of initial conditions distributed over a line in the $a - e$ plane close to the left branch of the resonance separatrix. For each initial condition, the initial angles $\theta = 2\sigma$ and $\Delta\varpi$ were distributed between 0 and 2π. Testing different values of the migration rate, we arrive to the following results:

- For the fastest migration rates (i.e. highly non-adiabatic regime) almost all the asteroids are able to cross the resonance without being captured. The first captured orbits appear in the elliptic and secular elliptic models for values of $\dot{a}_Y = 5.0 \times 10^{-4}$ AU/yr ($D = 0.05$ cm) and slower ones. For the circular model, captures start at $\dot{a}_Y = 2.5 \times 10^{-4}$ AU/yr ($D = 0.1$ cm).

- For the non-adiabatic case, we obtained similar results to those of Gomes (1995). The capture probability increases for increasing eccentricity until it reaches a maximum value (always less than 1) at an eccentricity e_{max}. From this value on, the probability decreases for increasing eccentricity, tending asymptotically to zero. Nevertheless, we observe several fluctuations along the probability curve due to the presence of the above mentioned capture windows. These fluctuation tend to disappear as we approach the adiabatic case.
- The limit between the non-adiabatic and adiabatic regimes occurs for $\dot{a}_Y = 2.5 \times 10^{-7}$ AU/yr ($D = 1$ m) in the circular model, and for $\dot{a}_Y = 5.0 \times 10^{-6}$ AU/yr ($D = 5$ cm) in the elliptic and secular elliptic models.
- For both the adiabatic and non-adiabatic regimes, our capture probabilities show a behavior similar to that described by Quillen (2006), even though her model significantly differs from ours.

We computed the total capture probability as a function of the migration rate, by integrating over a range of eccentricities. Along the range $0 \leq e \leq 0.4$, we obtained that, in the adiabatic limit, the probability tends to 40% in the circular model and to 30% in the other models. Restricting the integral to the range $0 \leq e \leq 0.04$, we found that the total capture probability is 100% for a migration rate of $\dot{a}_Y = 5.0 \times 10^{-7}$ AU/yr ($D = 50$ cm) in the circular model, and for $\dot{a}_Y = 5.0 \times 10^{-6}$ AU/yr ($D = 5$ cm) in the elliptic models. It is worth noting that these rates are compatible with the rates at which the transition between the non-adiabatic and adiabatic regimes actually occur. On the other hand, integrating over the interval $0.04 \leq e \leq 0.4$, the capture probability tend to 30 % in the adiabatic limit, independently of the model. All these percentages are approximate, and have been estimated from the outcome of a series of simulations for each system. A complete error estimation is beyond the scope of this paper, and not necessary for the current discussion.

Finally, integrating over the range of eccentricities typical of the Vesta family, $0.07 \leq e \leq 0.14$, we found that in the circular model the capture probability tend to 50 % for $\dot{a}_Y \leq 5.0 \times 10^{-6}$ AU/yr (i.e., $D > 5$ cm). However, in the elliptic models the probability is at least 87 % and 96 %, respectively, for $\dot{a}_Y \leq 1.0 \times 10^{-9}$ AU/yr (corresponding to $D > 250$ m). This result is in agreement with those of Roig et al (2008), who found that the capture probability of real asteroids under the perturbation of a full Solar System model is about 97 %. We conclude that the high capture probability of Vesta family members into the J3:1 MMR is basically governed by the eccentricity of Jupiter and its secular variations. The direct perturbations of other planets over the asteroids can be disregarded in the description of this phenomenon.

Acknowledgements The authors wish to thank Mira Broz and one anonymous referee for their comments and suggestions that helped to improve the manuscript. This work has been supported by CNPq and FAPERJ (Brazil) and CONICET (Argentina).

References

Asphaug, E.: Impact origin of the Vesta family. Meteor. Plan. Sci. **32**, 965–980 (1997). DOI 10.1111/j.1945-5100.1997.tb01584.x

Binzel, R.P., Xu, S.: Chips off of asteroid 4 Vesta - Evidence for the parent body of basaltic achondrite meteorites. Science **260**, 186–191 (1993). DOI 10.1126/science.260.5105.186

Borderies, N., Goldreich, P.: A simple derivation of capture probabilities for the J + 1 : J and J + 2 : J orbit-orbit resonance problems. Celest. Mech. **32**, 127–136 (1984). DOI 10.1007/BF01231120

Bottke Jr., W.F., Vokrouhlický, D., Rubincam, D.P., Broz, M.: The Effect of Yarkovsky Thermal Forces on the Dynamical Evolution of Asteroids and Meteoroids. Asteroids III pp. 395–408 (2002)

Burbine, T.H., Buchanan, P.C., Binzel, R.P., Bus, S.J., Hiroi, T., Hinrichs, J.L., Meibom, A., McCoy, T.J.: Vesta, Vestoids, and the howardite, eucrite, diogenite group: Relationships and the origin of spectral differences. Meteor. Plan. Sci. **36**, 761–781 (2001). DOI 10.1111/j.1945-5100.2001.tb01915.x

Bus, S.J., Binzel, R.P.: Phase II of the Small Main-Belt Asteroid Spectroscopic Survey: A Feature-Based Taxonomy. Icarus **158**, 146–177 (2002). DOI 10.1006/icar.2002.6856

Carruba, V., Michtchenko, T.A., Roig, F., Ferraz-Mello, S., Nesvorný, D.: On the V-type asteroids outside the Vesta family. I. Interplay of nonlinear secular resonances and the Yarkovsky effect: the cases of 956 Elisa and 809 Lundia. Astron. Astrophys. **441**, 819–829 (2005). DOI 10.1051/0004-6361:20053355

Carruba, V., Roig, F., Michtchenko, T.A., Ferraz-Mello, S., Nesvorný, D.: Modeling close encounters with massive asteroids: a Markovian approach. An application to the Vesta family. Astron. Astrophys. **465**, 315–330 (2007). DOI 10.1051/0004-6361:20066056

Cordeiro, R.R., Gomes, R.S., Vieira Martins, R.: A Mapping for Nonconservative Systems. Cel. Mech. Dyn. Astr. **65**, 407–419 (1996). DOI 10.1007/BF00049504

Cruikshank, D.P., Tholen, D.J., Bell, J.F., Hartmann, W.K., Brown, R.H.: Three basaltic earth-approaching asteroids and the source of the basaltic meteorites. Icarus **89**, 1–13 (1991). DOI 10.1016/0019-1035(91)90083-6

Delisle, J.B., Laskar, J.: Chaotic diffusion of the Vesta family induced by close encounters with massive asteroids. Astron. Astrophys. **540**, A118 (2012). DOI 10.1051/0004-6361/201118339

DeMeo, F.E., Binzel, R.P., Slivan, S.M., Bus, S.J.: An extension of the Bus asteroid taxonomy into the near-infrared. Icarus **202**, 160–180 (2009). DOI 10.1016/j.icarus.2009.02.005

Duffard, R., Roig, F.: Two new V-type asteroids in the outer Main Belt? Planet. Space Sci. **57**, 229–234 (2009). DOI 10.1016/j.pss.2008.07.009

Farinella, P., Vokrouhlicky, D., Hartmann, W.K.: Meteorite Delivery via Yarkovsky Orbital Drift. Icarus **132**, 378–387 (1998). DOI 10.1006/icar.1997.5872

Ferraz-Mello, S.: A Symplectic Mapping Approach to the Study of the Stochasticity in Asteroidal Resonances. Cel. Mech. Dyn. Astr. **65**, 421–437 (1996). DOI 10.1007/BF00049505

Ferraz-Mello, S., Klafke, J.C.: A model for the study of very-high-eccentricity asteroidal motion: the 3:1 resonance. In: S. Roeser, U. Bastian (eds.) Predictability, Stability, and Chaos in N-Body Dynamical Systems, pp. 177–184 (1991)

Ferraz-Mello, S., Klafke, J.C., Michtchenko, T.A., Nesvorný, D.: Chaotic Transitions in Resonant Asteroidal Dynamics. Cel. Mech. Dyn. Astr. **64**, 93–105 (1996). DOI 10.1007/BF00051608

Gomes, R.S.: Resonance Trapping and Evolution of Particles Subject to Poynting-Robertson Drag: Adiabatic and Non-Adiabatic Approaches. Cel. Mech. Dyn. Astr. **61**, 97–113 (1995). DOI 10.1007/BF00051690

Hadjidemetriou, J.D.: A hyperbolic twist mapping model for the study of asteroid orbits near the 3:1 resonance. J. Appl. Math. Phys. **37**, 776–796 (1986). DOI 10.1007/BF00947922

Hadjidemetriou, J.D.: Mapping models for Hamiltonian systems with application to resonant asteroid motion. In: S. Roeser, U. Bastian (eds.) Predictability, Stability, and Chaos in N-Body Dynamical Systems, pp. 157–175 (1991)

Hadjidemetriou, J.D.: Asteroid motion near the 3:1 resonance. Cel. Mech. Dyn. Astr. **56**, 563–599 (1993). DOI 10.1007/BF00696186

Henrard, J.: Capture into resonance - an extension of the use of adiabatic invariants. Celest. Mech. **27**, 3–22 (1982). DOI 10.1007/BF01228946

Henrard, J., Lemâitre, A.: A second fundamental model for resonance. Celest. Mech. **30**, 197–218 (1983). DOI 10.1007/BF01234306

Hiroi, T., Pieters, C.M.: Origin of vestoids suggested from the space weathering trend in the visible reflectance spectra of HED meteorites and lunar soils. Antarctic Meteor. Res. **11**, 163 (1998)

Lazzaro, D., Michtchenko, T., Carvano, J.M., Binzel, R.P., Bus, S.J., Burbine, T.H., Mothé-Diniz, T., Florczak, M., Angeli, C.A., Harris, A.W.: Discovery of a Basaltic Asteroid in the Outer Main Belt. Science **288**, 2033–2035 (2000). DOI 10.1126/science.288.5473.2033

Lemâitre, A.: High-order resonances in the restricted three-body problem. Celest. Mech. **32**, 109–126 (1984). DOI 10.1007/BF01231119

Malhotra, R.: Capture probabilities for secondary resonances. Icarus **87**, 249–264 (1990). DOI 10.1016/0019-1035(90)90133-T

McCord, T.B., Adams, J.B., Johnson, T.V.: Asteroid Vesta: Spectral Reflectivity and Compositional Implications. Science **168**, 1445–1447 (1970). DOI 10.1126/science.168.3938.1445

Migliorini, F., Morbidelli, A., Zappala, V., Gladman, B.J., Bailey, M.E., Cellino, A.: Vesta fragments from v6 and 3:1 resonances: Implications for V-type NEAs and HED meteorites. Meteor. Plan. Sci. **32**, 903–916 (1997). DOI 10.1111/j.1945-5100.1997.tb01580.x

Moskovitz, N.A., Jedicke, R., Gaidos, E., Willman, M., Nesvorný, D., Fevig, R., Ivezić, Ž.: The distribution of basaltic asteroids in the Main Belt. Icarus **198**, 77–90 (2008). DOI 10.1016/j.icarus.2008.07.006

Moskovitz, N.A., Lawrence, S., Jedicke, R., Willman, M., Haghighipour, N., Bus, S.J., Gaidos, E.: A Spectroscopically Unique Main-Belt Asteroid: 10537 (1991 RY16). Astrophys. J. Lett. **682**, L57–L60

(2008). DOI 10.1086/591030
Mothé-Diniz, T., Roig, F., Carvano, J.M.: Reanalysis of asteroid families structure through visible spectroscopy. Icarus **174**, 54–80 (2005). DOI 10.1016/j.icarus.2004.10.002
Murray, C.D., Dermott, S.F.: Solar system dynamics. Cambridge University Press, Cambridge (1999)
Mustill, A.J., Wyatt, M.C.: A general model of resonance capture in planetary systems: first- and second-order resonances. Mon. Not. RAS **413**, 554–572 (2011). DOI 10.1111/j.1365-2966.2011.18201.x
Neishtadt, A.I.: Passage through a separatrix in a resonance problem with a slowly-varying parameter. J. Appl. Math. Mech. **39**, 621–632 (1975)
Nesvorný, D., Roig, F., Gladman, B., Lazzaro, D., Carruba, V., Mothé-Diniz, T.: Fugitives from the Vesta family. Icarus **193**, 85–95 (2008). DOI 10.1016/j.icarus.2007.08.034
Nobili, A.M., Milani, A., Carpino, M.: Fundamental frequencies and small divisors in the orbits of the outer planets. Astron. Astrophys. **210**, 313–336 (1989)
Quillen, A.C.: Reducing the probability of capture into resonance. Mon. Not. RAS **365**, 1367–1382 (2006). DOI 10.1111/j.1365-2966.2005.09826.x
Roig, F., Ferraz-Mello, S.: A symplectic mapping approach of the dynamics of the Hecuba gap. Planet. Space Sci. **47**, 653–664 (1999). DOI 10.1016/S0032-0633(99)00009-4
Roig, F., Gil-Hutton, R.: Selecting candidate V-type asteroids from the analysis of the Sloan Digital Sky Survey colors. Icarus **183**, 411–419 (2006). DOI 10.1016/j.icarus.2006.04.002
Roig, F., Nesvorný, D., Gil-Hutton, R., Lazzaro, D.: V-type asteroids in the middle main belt. Icarus **194**, 125–136 (2008). DOI 10.1016/j.icarus.2007.10.004
Tholen, D.J.: Asteroid taxonomy from cluster analysis of Photometry. Ph.D. thesis, Arizona Univ., Tucson. (1984)
Thomas, P.C., Binzel, R.P., Gaffey, M.J., Storrs, A.D., Wells, E.N., Zellner, B.H.: Impact excavation on asteroid 4 Vesta: Hubble Space Telescope results. Science **277**, 1492–1495 (1997). DOI 10.1126/science.277.5331.1492
Vokrouhlický, D.: A complete linear model for the Yarkovsky thermal force on spherical asteroid fragments. Astron. Astrophys. **344**, 362–366 (1999)
Vokrouhlický, D., Farinella, P.: Efficient delivery of meteorites to the Earth from a wide range of asteroid parent bodies. Nature **407**, 606–608 (2000)
Wisdom, J.: The origin of the Kirkwood gaps - A mapping for asteroidal motion near the 3/1 commensurability. Astron. J. **87**, 577–593 (1982). DOI 10.1086/113132
Yoder, C.F.: Diagrammatic theory of transition of pendulum like systems. Celest. Mech. **19**, 3–29 (1979). DOI 10.1007/BF01230171

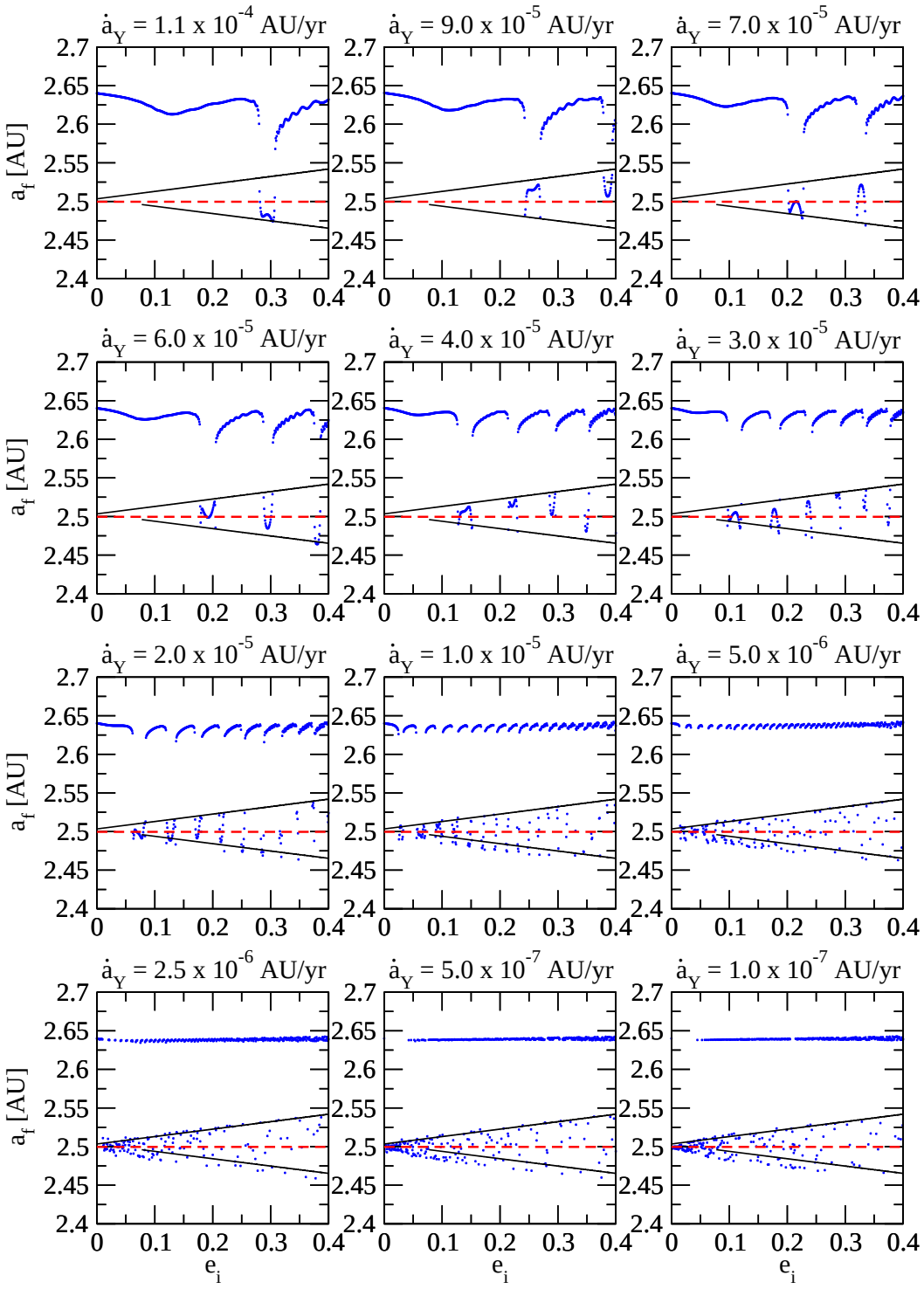

Fig. 2: Final semimajor axis vs. initial eccentricity obtained with the mapping equations for the circular problem ($e_1 = 0$), showing the structure of capture and crossing windows at fast migration rates. The initial angles are set to $\theta = \Delta\varpi = 0$. The migration rate decreases from left to right and from top to bottom. The separatrix (black curves) and center (red dashed) of the J3:1 MMR are indicated. This behavior is also observed in the elliptic case, and also with the numerical integration of the full Hamiltonian.

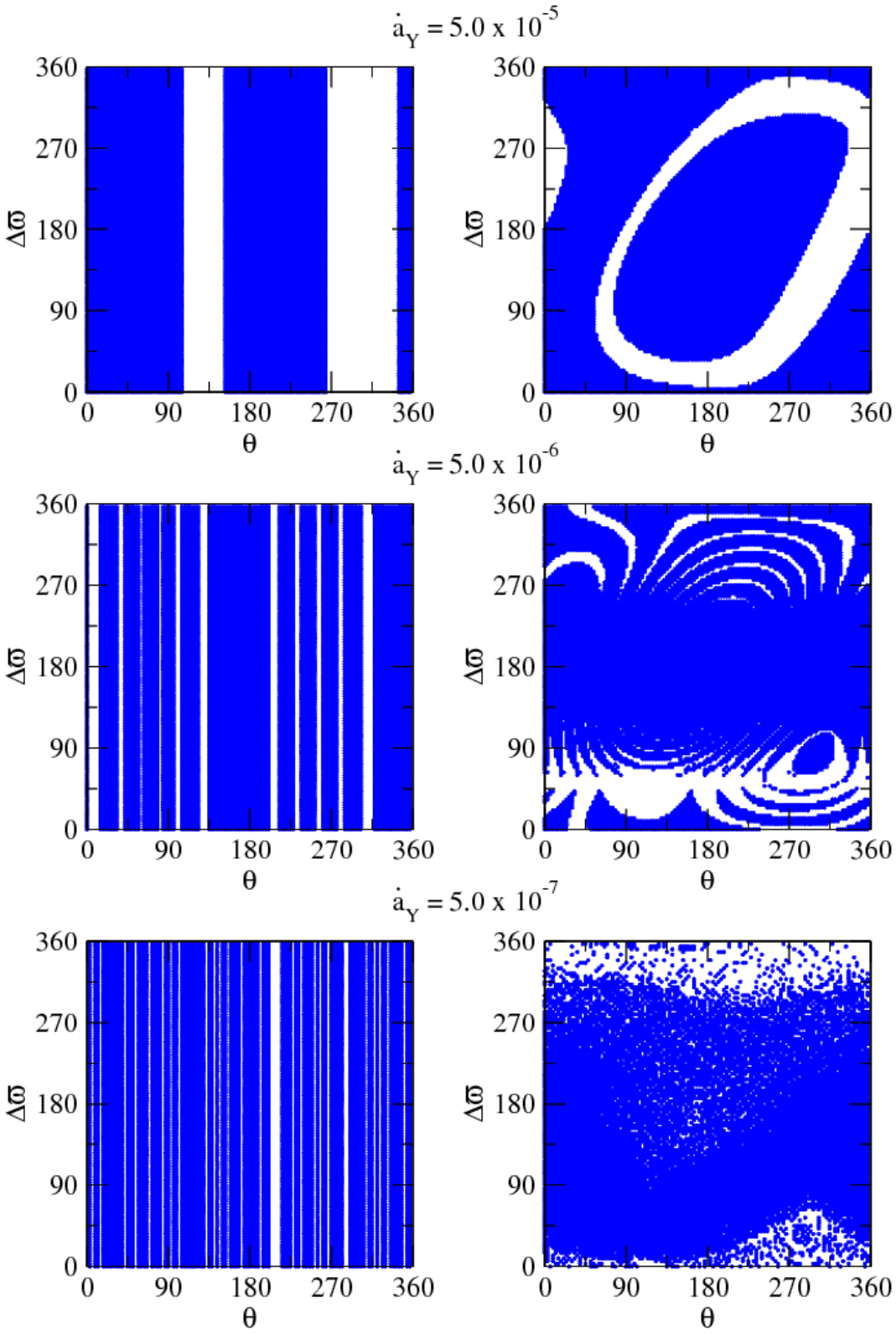

Fig. 3: Capture regions (in white) depending on the initial angles $\theta = 2\sigma$ and $\Delta\varpi = \sigma + \nu$ for a test orbit with initial $a = 2.45$ AU and $e = 0.2$. The left panels correspond to the circular model ($e_1 = 0$), while the right panels correspond to the secular elliptic model (see Sect. 3.2). The considered drift rates are indicated above the panels. Angles are in degrees.

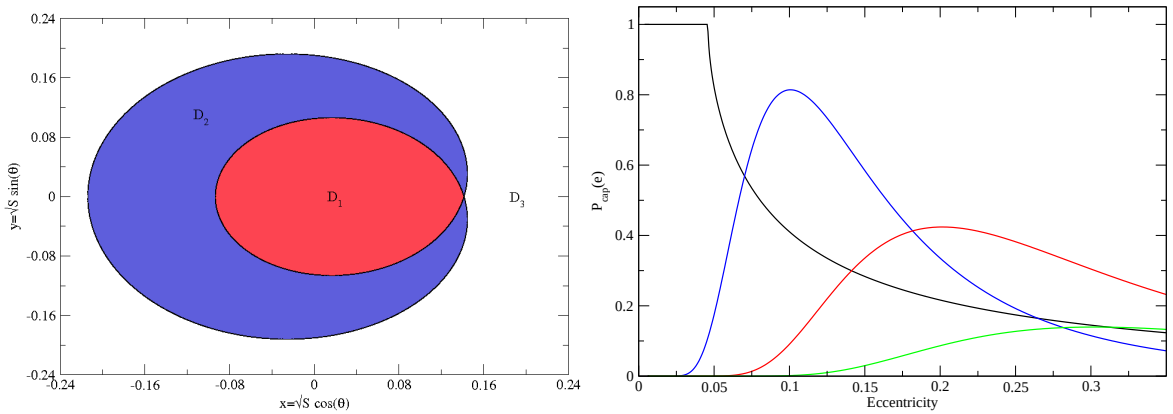

Fig. 4: *Left:* Schematic representation in the plane $x = \sqrt{S}\cos(\theta)$, $y = \sqrt{S}\sin(\theta)$ of a resonant, one degree of freedom, system with action-angle variables (S, θ). Region D_1 corresponds to a regime of inner circulation of θ; region D_2 corresponds to a libration around $\theta = \pi$; and region D_3 corresponds to an outer circulation. *Right:* Capture probability as a function of the eccentricity in the adiabatic case (black curve) and in three non adiabatic cases (blue, red and green curves). The green curve corresponds to the fastest migration rate. For slower migration rates, the location of the maximum shifts to smaller eccentricities, and the maximum probability grows until reaching the adiabatic case.

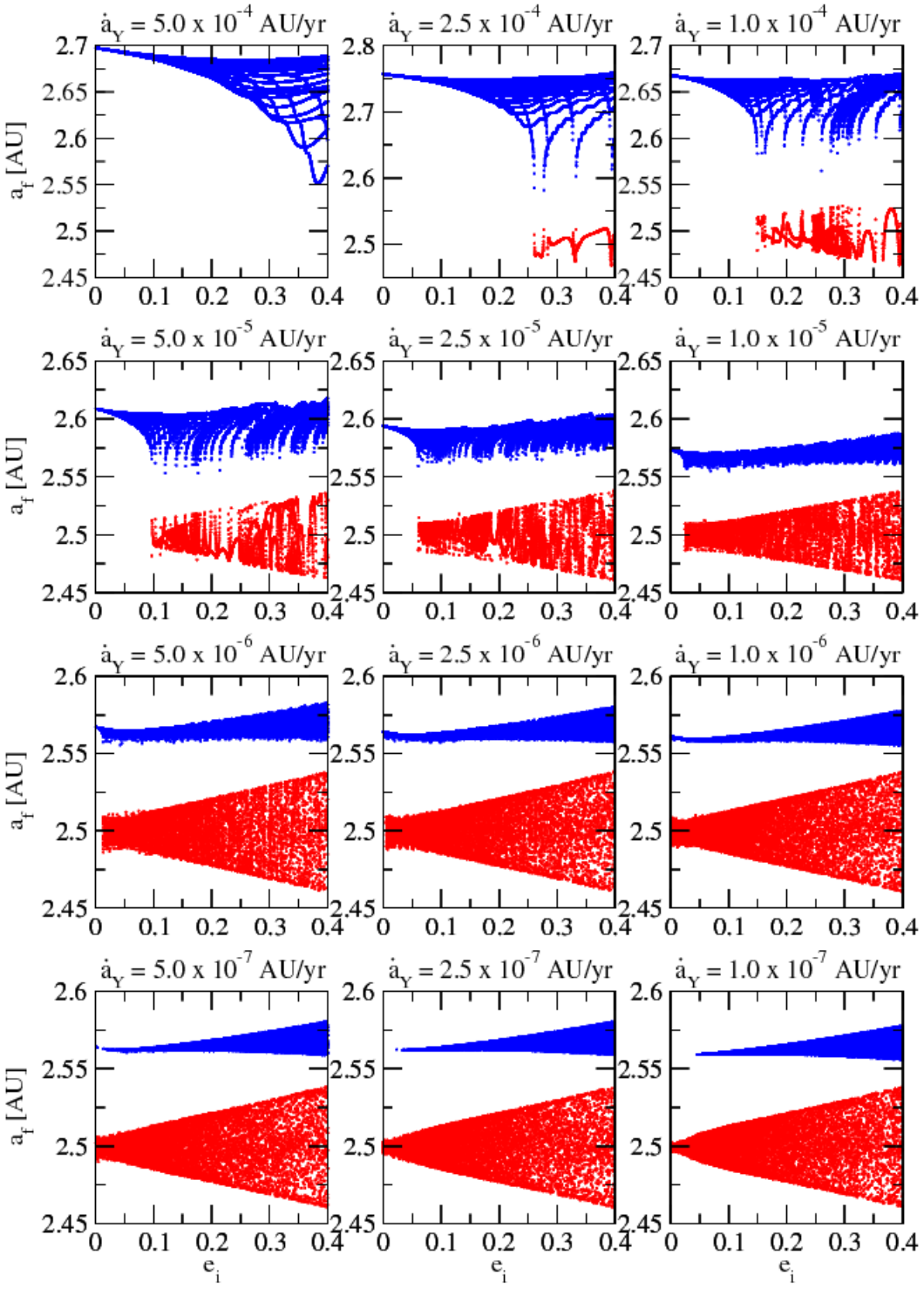
$\dot{a}_Y$ = 5.0 x 10^{-4} AU/yr
$\dot{a}_Y$ = 2.5 x 10^{-4} AU/yr
$\dot{a}_Y$ = 1.0 x 10^{-4} AU/yr
$\dot{a}_Y$ = 5.0 x 10^{-5} AU/yr
$\dot{a}_Y$ = 2.5 x 10^{-5} AU/yr
$\dot{a}_Y$ = 1.0 x 10^{-5} AU/yr
$\dot{a}_Y$ = 5.0 x 10^{-6} AU/yr
$\dot{a}_Y$ = 2.5 x 10^{-6} AU/yr
$\dot{a}_Y$ = 1.0 x 10^{-6} AU/yr
$\dot{a}_Y$ = 5.0 x 10^{-7} AU/yr
$\dot{a}_Y$ = 2.5 x 10^{-7} AU/yr
$\dot{a}_Y$ = 1.0 x 10^{-7} AU/yr
a_f [AU]
e_i

Fig. 5: Final semimajor axes vs. initial eccentricity obtained from the numerical simulations with the mapping assuming Jupiter in a circular orbit (model CM). Red dots represent captures while blue dots represent crossings. The migration rate $\dot{a}_Y$ decreases from left to right and from top to bottom.

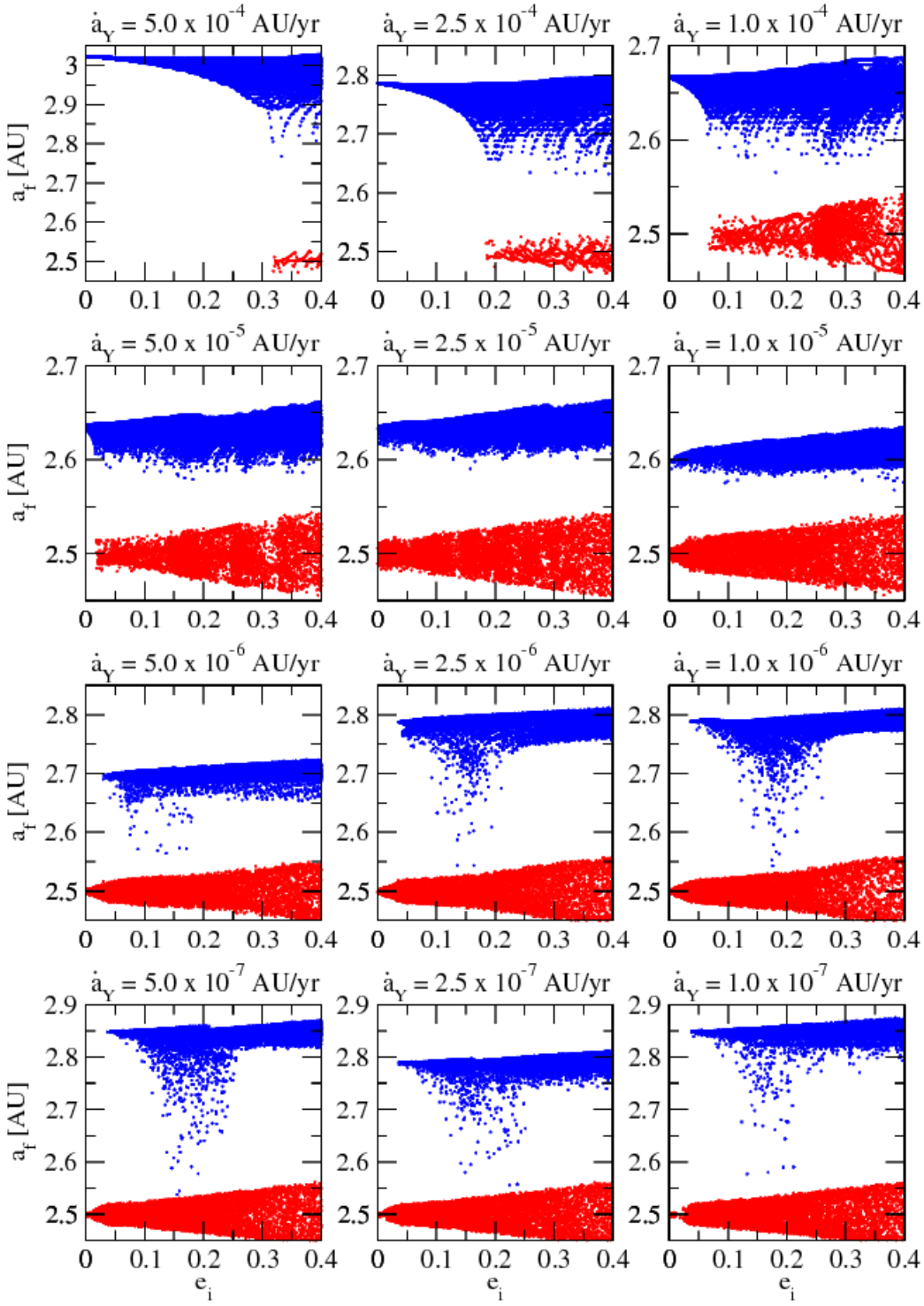
$\dot{a}_Y$ = 5.0 x 10^{-4} AU/yr
$\dot{a}_Y$ = 2.5 x 10^{-4} AU/yr
$\dot{a}_Y$ = 1.0 x 10^{-4} AU/yr
$\dot{a}_Y$ = 5.0 x 10^{-5} AU/yr
$\dot{a}_Y$ = 2.5 x 10^{-5} AU/yr
$\dot{a}_Y$ = 1.0 x 10^{-5} AU/yr
$\dot{a}_Y$ = 5.0 x 10^{-6} AU/yr
$\dot{a}_Y$ = 2.5 x 10^{-6} AU/yr
$\dot{a}_Y$ = 1.0 x 10^{-6} AU/yr
$\dot{a}_Y$ = 5.0 x 10^{-7} AU/yr
$\dot{a}_Y$ = 2.5 x 10^{-7} AU/yr
$\dot{a}_Y$ = 1.0 x 10^{-7} AU/yr
a_f [AU]
e_i

Fig. 6: Same as Fig. 5 but for Jupiter in a fixed elliptic orbit (EM). Note the tail of "delayed" crossings that appears between $0.1 < e < 0.2$ for the slowest migration rates (last six panels).

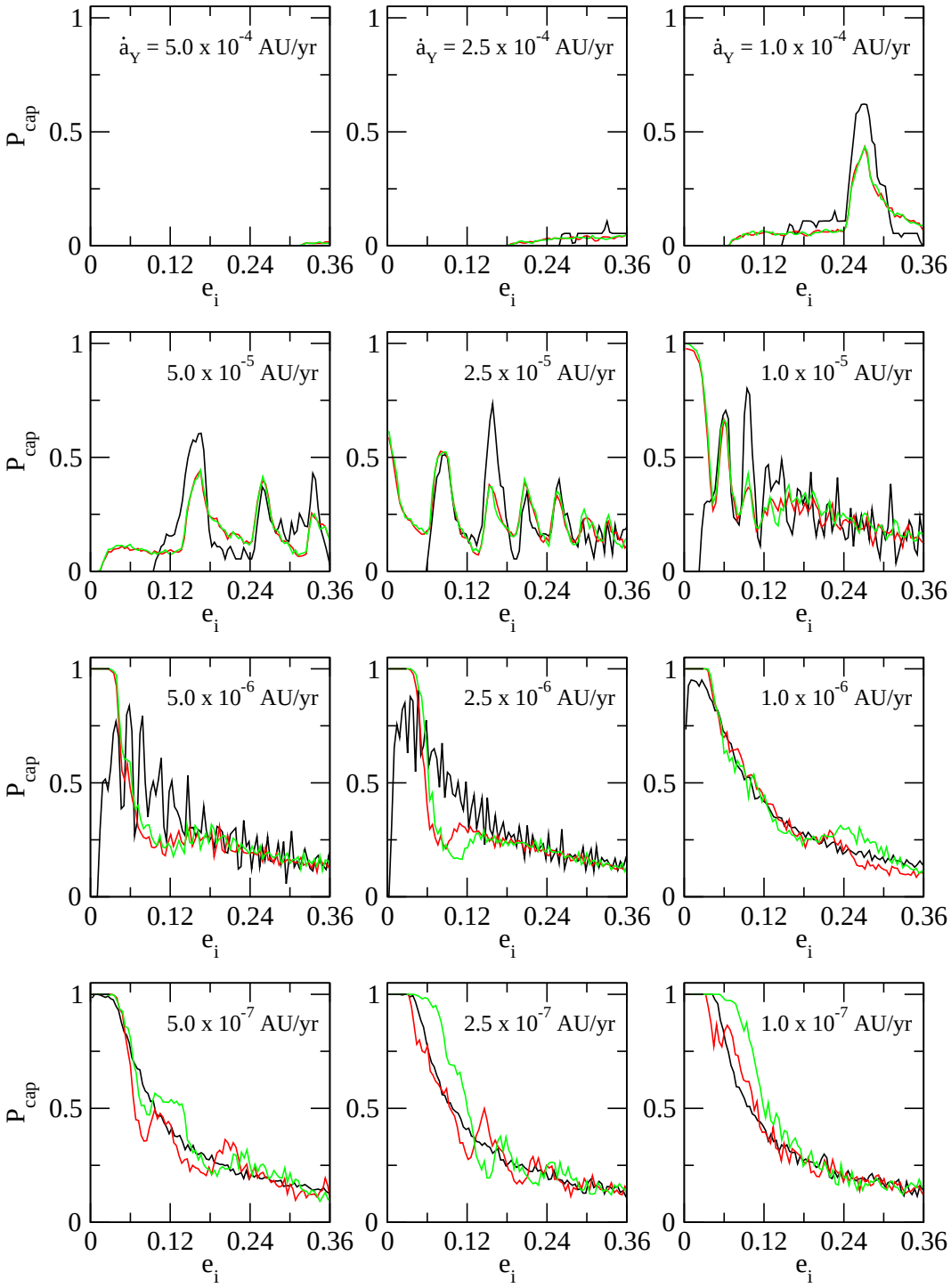

Fig. 7: Capture probability as a function of the initial eccentricity computed from the simulations shown in Figs. 5 (CM) and 6 (EM), plus results from the secular elliptic model (SEM). The black curve corresponds to the CM, red to the EM, and green to the SEM. The migration rate decreases from left to right and from top to bottom. For each initial eccentricity, the computed probability is "averaged" over the resonant angles $\theta, \Delta\varpi$.

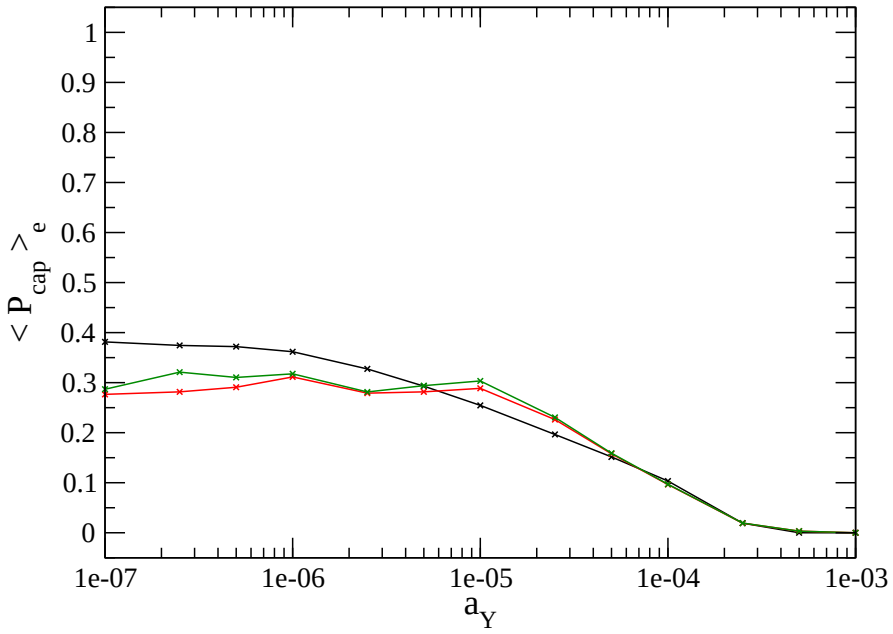

Fig. 8: Capture probability integrated over the angles and e, as a function of the migration rate. The black curve corresponds to the CM, red to the EM and green to the SEM.

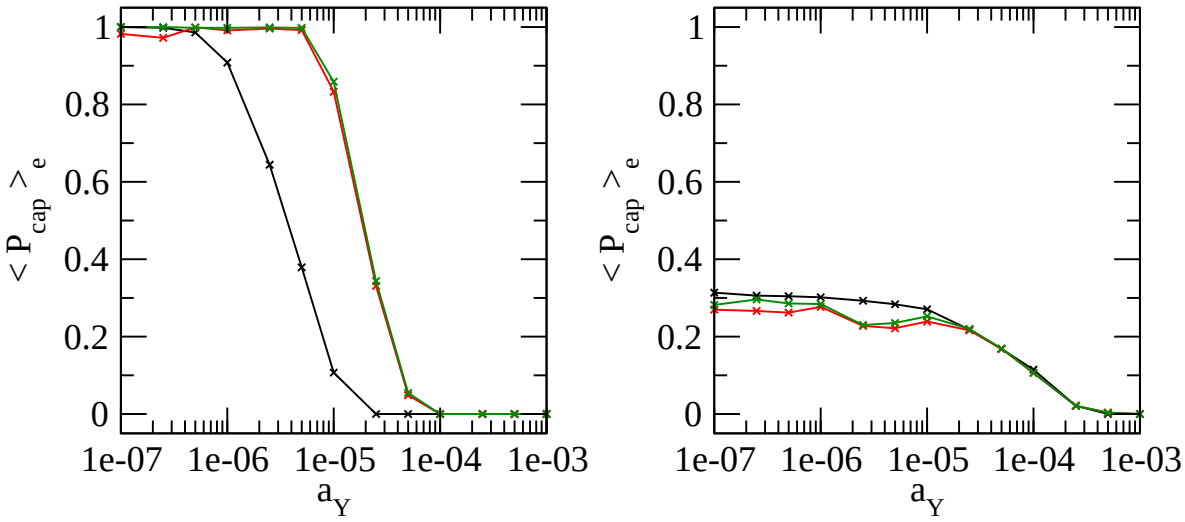

Fig. 9: Same as Fig. 8, but for two different intervals of e. *Left:* Very low eccentricities. *Right:* Intermediate to high eccentricities.

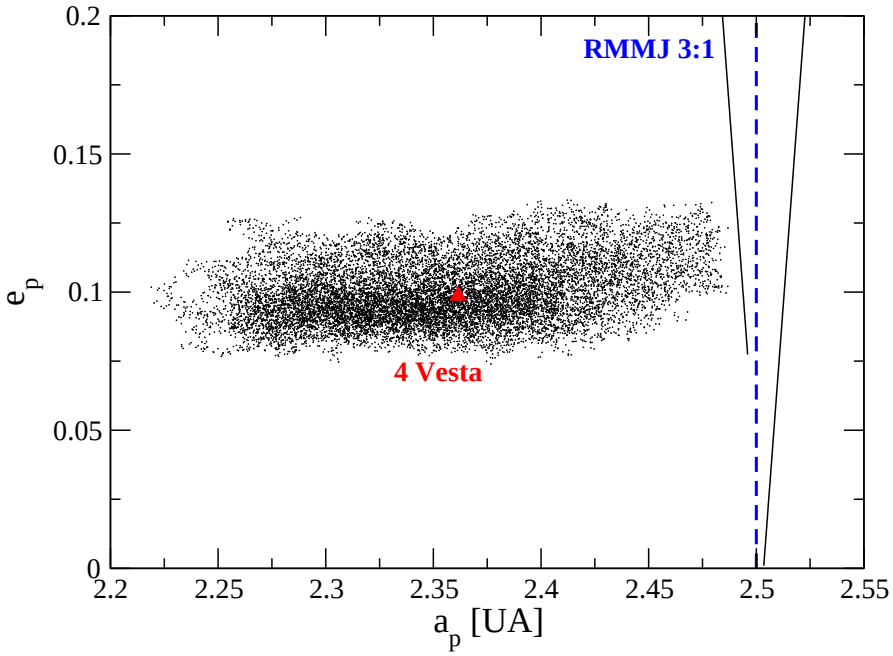

Fig. 10: The distribution of Vesta family asteroids on the plane of proper elements $a_p - e_p$ (black dots). The red triangle indicates the current location of 4 Vesta. The resonance separatrix (black lines) and center (blue dashed) are also shown. We are particularly interested on the evolution of family members close to the resonance border.

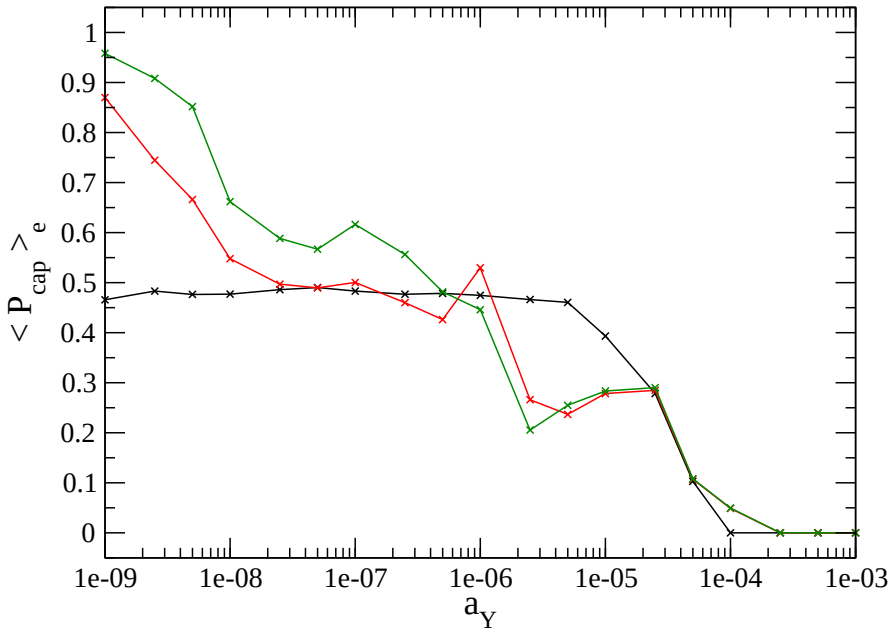

Fig. 11: Same as Fig. 8, but with the probability integrated between the eccentricity limits of the Vesta family (0.07 to 0.14). At the adiabatic limit ($\dot{a}_Y < 10^{-9}$) both the EM and the SEM predicts capture probabilities above 90–95 %, in good agreement with the results of Roig et al (2008).